High Harmonics and Isolated Attosecond Pulses from MgO

Zahra Nourbakhsh[1,*] Nicolas Tancogne-Dejean[1,†] Hamed Merdji[2] and Angel Rubio[1,3,4,‡]

[1]*Max Planck Institute for the Structure and Dynamics of Matter, Luruper Chaussee 149, 22761 Hamburg, Germany*

[2]*LIDYL, CEA, CNRS, Université Paris-Saclay, CEA Saclay, 91191 Gif sur Yvette, France*

[3]*Departamento de Fisica de Materiales, Nano-Bio Spectroscopy Group and ETSF, Universidad del País Vasco UPV/EHU, 20018 San Sebastián, Spain*

[4]*Center for Computational Quantum Physics, The Flatiron Institute, 162 Fifth Avenue, New York, New York 10010, USA*

On the basis of real-time *ab initio* calculations, we study the nonperturbative interaction of two-color laser pulses with MgO crystal in the strong-field regime to generate isolated attosecond pulses from high-harmonic emissions from MgO crystal. In this regard, we examine the impact of the characteristics of the incident pules, such as its shape, intensity, and ellipticity, as well as the consequences of the crystal anisotropy on the emitted harmonics and their corresponding isolated attosecond pulses. Our calculations predict the creation of isolated attosecond pulses with a duration of approximately 300 as; in addition, using elliptical driving pulses, we show the generation of elliptical isolated attosecond pulses. Our work prepares the path for all-solid-state compact optical devices offering perspectives beyond traditional isolated attosecond pulses emitted from atoms.

I. INTRODUCTION

High-harmonic generation (HHG) is a nonlinear optical process as the result of a strong laser field interacting with an atom, a molecule, a plasma, or a crystal. In this phenomenon, the target system emits light at frequencies equal to integer multiples of the frequency of the driving laser in the multicycle regime. HHG was discovered in 1987 in gases and atomic systems [1,2]; it was extended to crystals in 2010 [3]. HHG is a promising research area from both fundamental and practical points of view. HHG is a source of coherent extreme-ultraviolet radiation that has pioneered numerous applications. In particular, HHG in atoms has established attosecond science. The creation of an isolated attosecond pulse (IAP) from a HHG light source in 2001 [4] was a milestone in HHG history and ultrafast technology. Since then, there have been continuous efforts to generate brighter and shorter IAPs from HHG sources [5]. IAPs can reveal microscopic

details of the physical processes involved, with attosecond-timescale resolution, such as electron motion in materials, bond creation or bond breaking, and other ultrafast, sub-optical-cycle quantum-mechanical phenomena [6–9].

Solid-state HHG has attracted much attention in recent years [10–31] due to the different possibilities in solids to control and tailor the HHG radiation properties. It is possible to act on the HHG emission by engineering the crystal structure, chemically or mechanically [11–16], or by rotating the target sample [23,24]. Additionally, the coupling between electrons and holes in crystals makes it possible for the excited electrons to recombine in neighboring sites [31]. Accordingly, solids could show a stronger response to an elliptical laser field in comparison with the gas phase, where the excited electrons need to recombine coherently with their parent ions; note that ellipticity behaviors in solids depend on the material symmetries [20–22]. Moreover, higher density [19] and electronic momentum change induced by lattice periodicity [22] can lead to a stronger HHG spectrum in solids; for instance, monoatomic crystals display a brighter HHG spectrum compared with their gas phases under the same incident pulse [30]. Furthermore, a high-harmonic response could inform about the electronic and dynamical properties of the solid system [10].

Following more than a decade of advances [32–35], the shortest IAP ever produced was achieved in 2017, with a duration of 43 as [36]. Despite these successes, the corresponding experimental techniques proposed for

---

*zahra.nourbakhsh@mpsd.mpg.de

†nicolas.tancogne-dejean@mpsd.mpg.de

‡angel.rubio@mpsd.mpg.de

generating IAPs are difficult to implement, and attempts toward producing more-accessible techniques are continuing. Controlling the driving pulse using two colors and tuning the second-pulse parameters in order to confine the emission probability in a shorter range of pulse duration was originally proposed in atoms and in a free-electron laser [37,38], and due to their potential applications to investigate electron ultrafast dynamics, they are widely used to tailor the harmonic emission of different systems ranging from gases to liquid and solids [39–45].

Besides the input-pulse properties, the target system and its strong-field response are very important to generate IAPs. In this article, we consider wide-band-gap MgO crystal as the target system. MgO is a well-known solid in the HHG community due to its high damage threshold with regard to intense ultrashort infrared input pulses. In addition, because of ionic bonds in MgO crystal, with a rock-salt structure, its inhomogeneous electron-nuclear potential is similar to that of atomic cases; consequently MgO crystal has the advantages [19] of both atomic and solid systems in one material.

Our demonstration is based on *ab initio* time-dependent density-functional theory (TDDFT) [46,47] implemented in the OCTOPUS package [48]. This method allows us to model the electron dynamics in solids without making strong assumptions and was shown to provide good agreement between simulation results and experimental measurements [20]. We show using two-color intense pulses that IAPs with a duration as short as approximately 300 as are extracted from the harmonic emission in the extreme-ultraviolet range. This is shorter than what was measured experimentally in SiO_2 nanofilm (470 as) [25] or the *ab initio* prediction of IAP duration in MoS_2 monolayer (2280 as) [26].

This paper is organized as follows. After our reviewing the theoretical method in the next section, we present our results in Sec. III. The effect of of the pulse strength, polarization direction, and two-color asymmetric pulses on HHG response as well as IAP creation is discussed in that section. We end Sec. III with the investigation of the ellipticity effect on HHG and IAP production. Finally, Sec. IV summarizes our main results.

II. METHOD

TDDFT calculations of the time evolution of the electronic wave functions are performed with the OCTOPUS code [48] on the basis of the Kohn-Sham equation, defined as

$$i\frac{\partial}{\partial t}\phi_i(\mathbf{r},t) = \left(-\frac{\nabla^2}{2} + v_{\text{ext}}(\mathbf{r},t) + v_H[n(\mathbf{r},t)] \right.$$
$$\left. + v_{xc}[n(\mathbf{r},t)]\right)\phi_i(\mathbf{r},t), \quad (1)$$

where $v_{\text{ext}}(\mathbf{r},t)$ is the external potential including the applied synthesized laser field and electron-ion potential, v_H is the Hartree part of the Coulomb electron-electron interaction, v_{xc} is the exchange-correlation potential, and $n(\mathbf{r},t)$ is the time-dependent electron density defined as $n(\mathbf{r},t) = \sum_i |\phi_i(\mathbf{r},t)|^2$, where ϕ_i is the Kohn-Sham orbital associated with the index i corresponding to both a band and a k-point index. In the next step, the total microscopic current, $\mathbf{j}(\mathbf{r},t)$, is computed from the time-dependent wave functions. Finally, the high-harmonic spectrum is obtained by the Fourier transform of the laser-driven electron current

$$\text{HHG}(\omega) = \left|\text{FT}\left(\frac{\partial}{\partial t}\int_\Omega d^3\mathbf{r}\,\mathbf{j}(\mathbf{r},t)\right)\right|^2, \quad (2)$$

where Ω is the system volume. The attosecond pulse can be extracted from the coherent superposition of consecutive harmonics [9]:

$$I(t) = \left|\sum_{\omega_i}^{\omega_f} e^{i\omega t}\text{FT}\left(\frac{\partial}{\partial t}\int_\Omega d^3\mathbf{r}\,\mathbf{j}(\mathbf{r},t')\right)\right|^2, \quad (3)$$

where ω_i and ω_f define the energy window used to calculate the IAP. Time-frequency analysis of high harmonics is performed with the Gabor transform [49] of HHG:

$$G_{\text{HHG}}(\tau,\omega) = \left|\int_{-\infty}^{\infty} dt \exp\left(\frac{-(t-\tau)^2}{2w^2}\right)\right.$$
$$\left. \times\, e^{-i\omega t}\left(\frac{\partial}{\partial t}\int_\Omega d^3\mathbf{r}\,\mathbf{j}(\mathbf{r},t)\right)\right|^2, \quad (4)$$

where the integral limitations practically reduce to the duration of our pulse, which is from 0 to 36 fs, and our time window w is taken to be 0.25 fs.

Unless stated otherwise, the exchange-correlation term is described by the local-density approximation (LDA); we use the set of norm-conserving Hartwigsen-Goedecker-Hutter LDA pseudopotentials [50]. While the LDA underestimates the band gap, it correctly describes the band dispersion of the valence and conduction bands [51], and thus is capable of describing properly the coupled interband and intraband dynamics. A dense k-point grid of $28 \times 28 \times 28$ and a grid spacing of 0.2 bohr are used thorough our calculations. We use a lattice constant of 4.18 Å for MgO crystal with a rock-salt structure.

III. RESULTS AND DISCUSSION

A. Linear polarized pulse: high-harmonic and IAP generation

1. One-color-pulse versus two-color-pulse HHG

We start our discussion by analyzing the nonperturbative interaction between our fundamental pulse, polarized

along the [100] direction, and the MgO crystal; the results are presented in Fig. 1. Our fundamental laser pulse is set to a wavelength of 1.8 μm. The intensity of a few 10^{12} W per square centimeter, corresponding to an electric field strength of approximately 0.6 V/Å in the bulk system, is kept below the damage threshold of MgO crystal. The pulse duration at the full width at half maximum (FWHM) is 18 fs, with a sine-squared envelope shape for the vector potential; the carrier-envelope phase of the fundamental pulse is set to zero.

The HHG spectrum, presented in Fig. 1(a), shows that odd harmonics up to a cutoff energy of approximately 22 eV are generated, while, because of the inversion symmetry in MgO crystal, even harmonics are absent here [3].

The mechanism of solid-state HHG is usually explained by interband and intraband dynamics [12,26–29]. The first four harmonics in Fig. 1(a), with energies below the DFT band gap, are generated by intraband acceleration, while for harmonics above the band gap, interband recombination can also contribute to the emission of harmonics. As a result, the spectrum above the band gap is noisier and not as clean as the HHG signal originating from intraband dynamics only. This behavior is discussed in more detail in Ref. [19] for bulk silicon.

The time-frequency analysis, presented in Fig. 1(b), predicts that no IAPs can be extracted from this harmonic spectrum, and as Fig. 1(c) shows, a train of attosecond pulses results from this emission. At lower energy (i.e., between 12 and 20 eV), the HHG emission is maximum and shows complex dynamics with evidence of a positive chirp of the attosecond bursts (see the dashed black lines).

The two-color results are illustrated in Fig. 2 [52]. The corresponding HHG spectra are displayed in Fig. S2 in Supplemental Material [53]. In this work, the pulse shape and HHG spectra are controlled with use of the second-color pulse strength, frequency, and phase. Practically, these characteristics are adjusted to control the attosecond electron dynamics within the MgO bands such

that the HHG is emitted only during a fraction of an optical cycle over the entire pulse. The driving two-color vector potential is defined as

$$\mathbf{A}(t) = \mathbf{A}_0 \sin^2(t\pi/\delta) \left[\sin \omega_0 t + \frac{e}{f} \sin(f \, \omega_0 t + \phi_2) \right],$$
(5)

where $\mathbf{A}_0$ and ω_0 are, respectively, the vector potential and frequency of the fundamental pulse, t is time, and the width δ is 36 fs, consisting of twice the pulse duration. The pulse polarization, duration, and envelope shape of the second laser field are the same as those of the fundamental pulse. IAPs are strongly governed by the effective detuning and dephasing of the second harmonic as shown in Fig. 2. This reveals the importance of an asymmetric pulse in IAP generation.

In Fig. 2, the total electric field strength increases from right to left; the peak field strength in Figs. 2(a) and 2(d) is respectively 1.7 V and 0.8 V/Å, respectively. This enhancement raises the emission intensity and extends the HHG cutoff energy from approximately 22 eV in Fig. 2(d) to approximately 42 eV in Fig. 2(a) (see Figs. S2 and S5 in Supplemental Material [53]). Practically, bright IAPs are produced slightly after the extremum of the vector potential, which corresponds to the strongest acceleration of the electron current in the conduction band. As indicated in Fig. 2, for each case according to its time-frequency spectrum, we reoptimize the energy window to obtain the shortest IAP possible from the harmonic emission, as one would do experimentally. The IAP duration reported in Fig. 2 (defined from the FWHM of the filtered signal) does not show any serious dependence on the electric field strength.

The IAP in Fig. 2(a) has a negative attosecond chirp for harmonics between 15 and 21 eV. The negative chirp sign is opposite the single-color case and the chirp usually
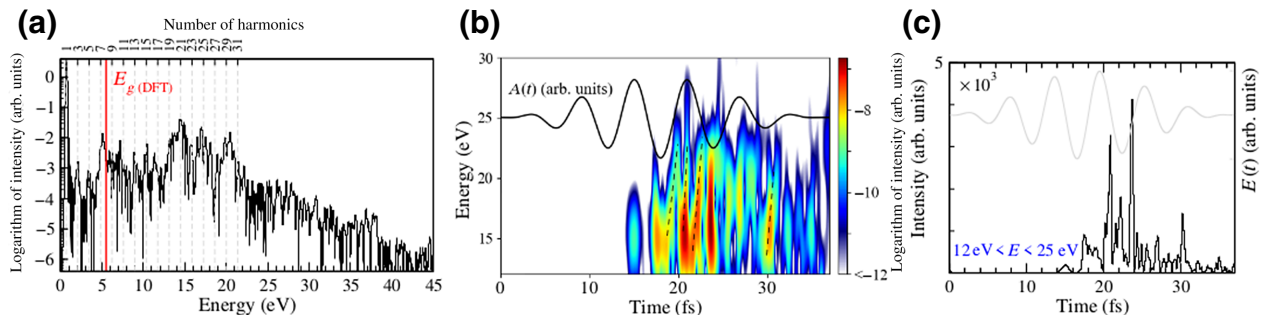

(a) **(b)** **(c)**

FIG. 1. (a) HHG spectrum corresponding to the fundamental laser; the pulse polarization is along the [100] direction. The dashed lines mark the harmonic frequencies. The solid red line indicates the MgO DFT band gap (5.4 eV). (b) Time-frequency analysis of the HHG. This figure also shows the time profile of the vector potential. The dashed black lines indicate the attosecond chirp. (c) A train of attosecond pulses resulting from the fundamental laser pulse for the given energy window. The time-dependent electric field is also displayed.
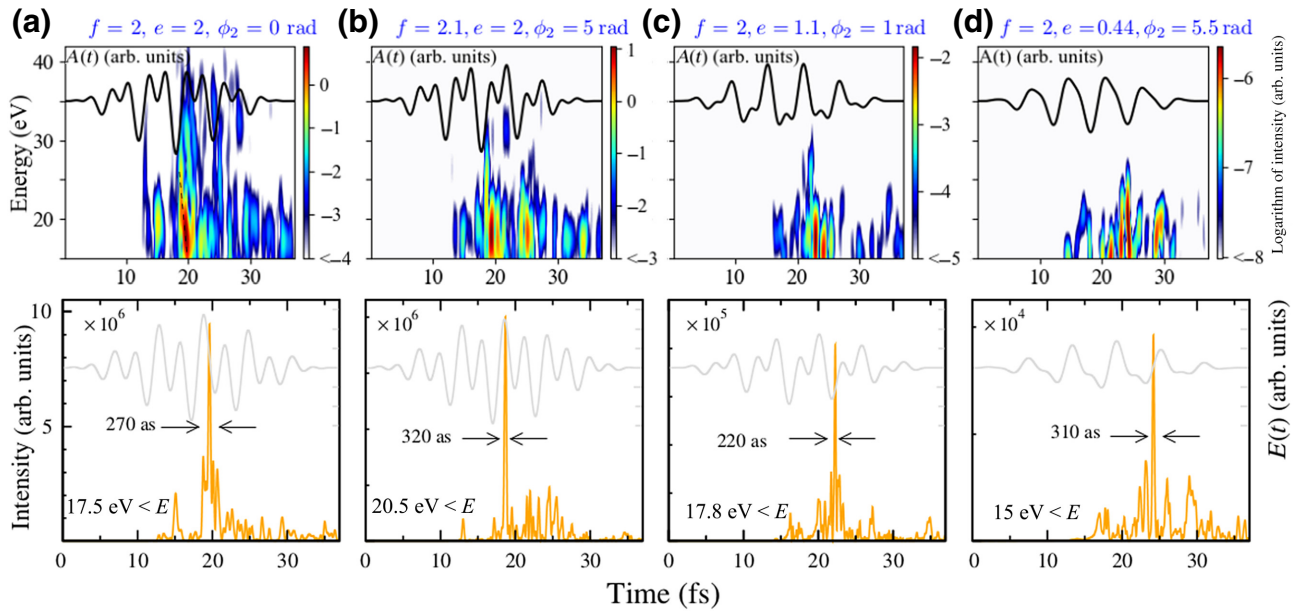
FIG. 2. Two-color-pulse time-frequency analysis (top row) and the related IAPs (bottom row). The results for four different two-color pulses are shown; the light polarization is along the [100] direction. The titles specify the pulse characteristics; e, f, and ϕ_2 are as defined in Eq. (5). The dashed black line in (a) shows a negative chirp. The IAP duration and the corresponding energy windows are given in the bottom panels. The minor spaces in the IAP diagrams are equal to 1 arb. unit and their scales are marked next to the axes. The total electric field profiles are shown in light gray in the bottom row, with the same scale used for the panels.

reported in gas HHG [54]. Besides the material, the properties of the pulse, such as its wavelength, strength, and shape, affect the chirp sign and magnitude. The fact that we can tailor the attosecond chirp under certain driving conditions can be used to control the attosecond pulses. Additionally, this could reveal details of the microscopic electron dynamics at the place, but a detailed study is beyond the scope of the present work.

Since DFT calculations performed at the level of the LDA or generalized-gradient approximation (GGA) underestimate the band gap, we also perform calculations using the TB09 meta-GGA functional [55], which yields an accurate estimation of the MgO band gap. The results presented in Fig. S1 in Supplemetal Metarial [53] imply that the band-gap enhancement does not affect significantly our main conclusions and shows the validity of using the LDA to study the generation of IAPs in MgO.

Our *ab initio* results for the IAP duration in MgO are shorter than what was obtained from TDDFT calculations in MoS$_2$ crystal with a FWHM duration of 2280 as [26]. This is also shorter than the IAP measured experimentally in SiO$_2$ nanofilms with a duration of 470 as resulting from a single-cycle pulse with a peak field strength of 1.1 V/Å. Moreover, the energy windows used to extract the IAPs, which are specified in the bottom row in Fig. 2, are much wider than the calculated bandwidth in MoS$_2$ (16–20 eV) [26] and that measured in SiO$_2$ (18–28 eV) [25]. For example, the filtering area in Fig. 2(a) starts from 17.5 eV and covers the extreme-ultraviolet energy range up to 43 eV.

Our results therefore show that MgO is a promising candidate for the generation of IAPs for solid targets. Finally, we note that a recent publication [56] on bulk MgO, using the one-dimensional semiconductor Bloch equation, predicts IAPs with a duration of 817–1000 as and a bandwidth of 20–35 eV for a two-cycle pulse with a wavelength of 1.6 μm.

Another point worth mentioning is the emission time of the intense attosecond pulses versus the electric-field and vector-potential extrema. For instance, in Fig. 2(a), the IAP is emitted at the vector-potential peak, while in Fig. 2(b), the IAP is emitted at the electric-field extremum; similar behaviors are seen in Fig. 1 or Fig. S4 in Supplemental Material [53]. Since within the dipole approximation $\mathbf{E}(t) \propto (\partial/\partial t)\mathbf{A}(t)$, the vector-potential extrema correspond to zeros of the electric field. This could arise from the different microscopic origins of the harmonics involved in each IAP. For instance, the intraband dynamics is a coherent emission occurring in phase with the driving electric field, and is enhanced when the band structure has its largest curvature or when the electric field is at its maximum [17]; in contrast, when the vector potential is maximum, the band gap increases and the emitted harmonics are dominated by interband dynamics [17].

We end this part by discussing the electric-field-strength and wavelength dependence of the HHG cutoff energy. In gases, this dependency is defined by the ponderomotive energy $U_p \propto \lambda^2 E_0^2$, but since the excited electrons in solids are not free particles in a continuum but quasifree
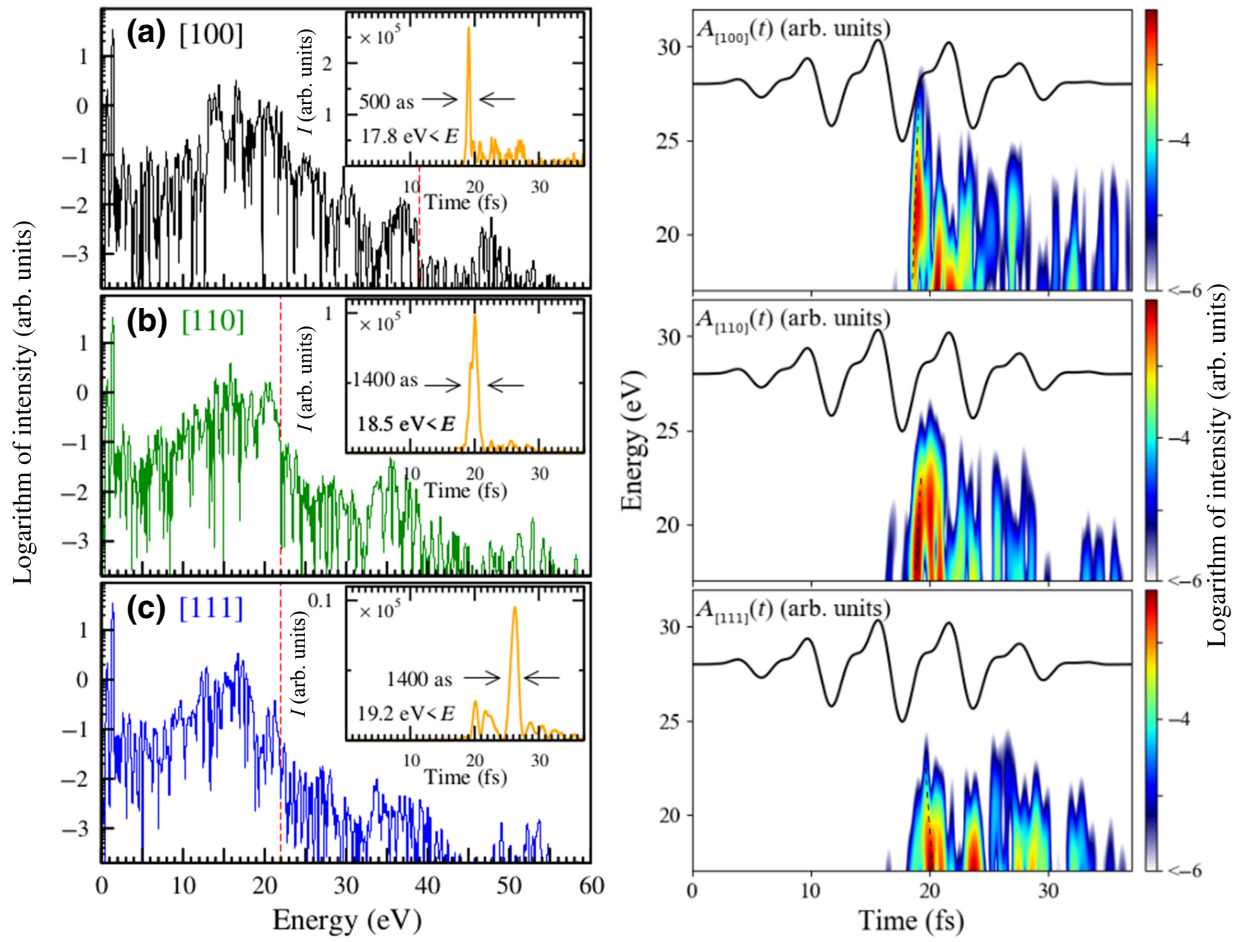
FIG. 3. The impact of the pulse polarization direction on high-harmonic and IAP generation. In the left panels, the pulse polarizations are along the [100], [110], and [111] directions from top to bottom. The dashed red lines specify the HHG cutoff energies. The inset plots show the corresponding IAPs. The right panels show the corresponding time-frequency analysis. Also, this figure shows the time profile of the vector potential. The dashed black lines allow the chirp of the pulse to be followed.

particles moving on energy bands, this equation is not generally valid for solids. As shown in Fig. S5 in Supplemental Material [53], we find that the harmonic cutoff scales linearly with the driving-pulse peak field. However, besides the electric field strength, the pulse shape affects the cutoff energy, and we find that asymmetric pulses yield shorter energy cutoffs than single-color pules. The opposite findings have been repoted for sensitivity [12,57,58] or insensitivity [11,19,59] of the cutoff energy to wavelength in solids; according to our results obtained for two different single-color pulses with wavelengths of 800 and 1800 nm (other pulse characteristics are the same as those of the fundamental pulse), the cutoff energy is found to be independent of the pulse wavelength in MgO (plots not shown).

2. Anisotropy impacts

The rest of our study on linearly polarized pulses in MgO focuses on the HHG response to the crystal anisotropy. Rotating the crystalline target or pulse polarization direction provides a way to manipulate the crystal harmonic emission, which is not accessible to atoms, as solids possess intrinsic symmetries that influence the dipole coupling strength and possible transitions between bands, thus changing interband and intraband dynamics, and consequently affecting the harmonic spectra.

Figure 3 shows MgO HHG spectra as well as the time-frequency profiles arising from the same driving pulses but with different polarization directions; for simplicity, we consider light polarization only along the high-symmetry [100], [110], and [111] directions. A two-color pulse is used to perform these calculations with $f = 2$, $e = 0.9$, and $\phi_2 = 1$ rad and the same polarization direction.

Regarding Fig. 3, the harmonic emission, especially for energies above 20 eV, is suppressed for the [110] and [111] directions. The much-stronger high-harmonic emission, for polarization along the [100] direction, can be roughly explained by the strong ionic potential along this direction
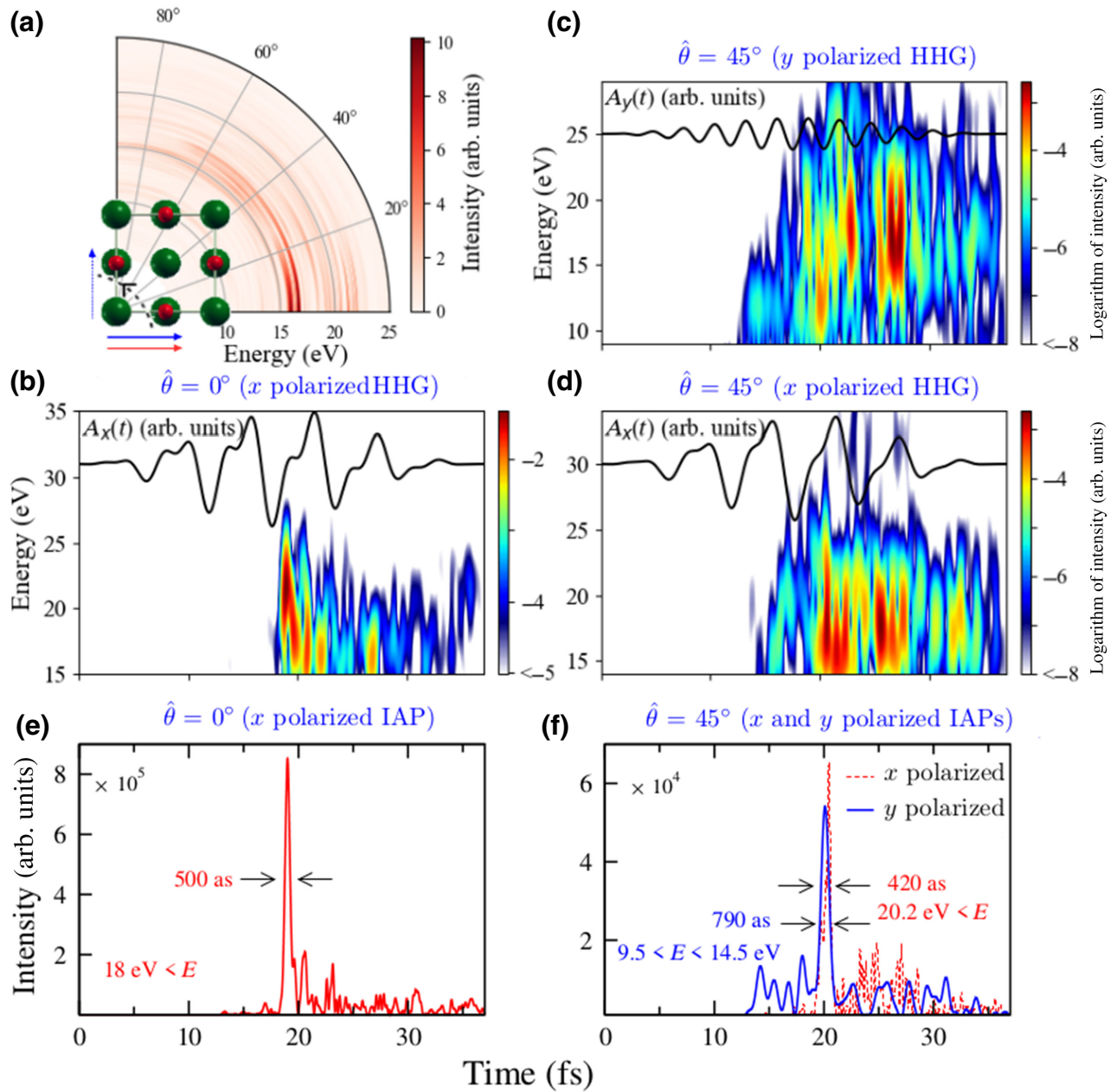
FIG. 4.   Ellipticity impact on high-harmonic and IAP generation. (a) Two-color-pulse HHG spectrum as a function of the second field polarization direction; the $0°$ direction corresponds to the [100] direction. (b)–(d) The polarization-resolved calculated time-frequency spectra: (b) for the nonrotated case or the linearly polarized two-color pulse; (c),(d) for the second field polarization rotation of $\theta = 45°$. The first and second rows show, respectively, the time-frequency plots for the y-polarized and x-polarized harmonics; for the nonrotated case displayed in (b), high harmonics are totally polarized along the pulse polarization direction (x direction here). The polarization-resolved vector-potential profiles are also shown, with the same scale used for the panels. (e),(f) The corresponding polarization-resolved IAPs.

(see Supplemental Material [53]). The potential along the [111] direction is also between Mg^{2+} and O^{2-} ions, but the distance between the ions in this direction is almost twice the bond length in the [100] direction. Figure 3 shows that the HHG spectra for the [110] and [111] directions have the same cutoff energies; however, the spectrum with polarization along the [110] direction is relatively more

intense. We note that the anisotropic HHG emission discussed here is consistent with fingings of previous studies on MgO [23,24].

The insets in Fig. 3 show the corresponding IAPs. The results imply that for the [110]- and [111]-polarized pulses, the length and contrast of IAP generation rapidly deteriorate compared to the [100]-polarized pulse. The [100] case

shows the brightest IAP and the shortest pulse duration, with a slight positive chirp. The [110] case demonstrates an attosecond pulse; however, the time-frequency representation shows that complex dynamics occurs with a pronounced positive chirp. The [111] case does not exhibit a well-contrasted IAP. The main pulse (at around 26 fs) has a prepulse with negative chirp (starting at 20 fs). Again, this illustrates the complex attosecond dynamics occurring within the MgO bands. We conclude that, in addition to the pulse asymmetry, the calculated IAPs are strongly influenced by the crystal orientation, which is an important difference compared with the atomic case.

B. Ellipticity impacts on high-harmonic and IAP generation

Use of linearly polarized two-color pulses allows the generation of customized elliptically polarized pulses by rotation of the polarization direction of one of the two pulses. To investigate the ellipticity impact on HHG and IAP generation in MgO, we perform calculations for noncollinear polarized drivers. Figure 4 summarizes our results for two-color laser pulses as a function of the second-pulse polarization angle. The direction-resolved time-frequency profiles and their corresponding IAPs are shown in Fig, 4. Our driving vector potential is $\mathbf{A}(t) = A_0 \sin^2(t\pi/\delta)[\sin(\omega_0 t)\hat{i} + (1/2.1)\sin(2.1\omega_0 t + 5.5)\hat{\theta}]$, where A_0 and ω_0 are, respectively, the fundamental-pulse vector potential and frequency, as defined in Sec. II.

The polar plot in Fig. 4(a) shows that by rotation of the second field, harmonic emissions continuously fall off; for instance, two intense harmonics with energies of approximately 16–17 eV drop by approximately an order of magnitude when the second pulse rotates from the parallel direction to the perpendicular direction. Besides, the cutoff energy decreases from 36 eV for the collinear case to 27 eV for a rotation angle of 45° and 25 eV for a rotation angle of 90°; more details are shown in Figs. S6 and S7 in Supplemental Material [53].

We now study the possibility of IAP generation for the second-pulse rotation angles of 45° and 90° as well as the collinear case (or 0°). The time-frequency plots and the corresponding IAP plots for the high-harmonic emission for the collinear case and for a rotation angle of 45° are shown in Figs. 4(b)–4(f); for 90° rotation (not shown), no clear IAP is obtained from either *x*-polarized or *y*-polarized high harmonics. The results presented in Fig. 4 for a rotation angle of 45° reveal the possibility of having an elliptical IAP resulting from the appropriate tuning of the different input parameters. As shown in Fig. 4(f), the *x*-polarized and *y*-polarized IAPs are emitted at the same time. Elliptical IAPs are usually cumbersome to generate

in gases and are important for studying spin-polarized electronic motion in molecular or condensed-matter systems [60,61].

IV. SUMMARY

By *ab initio* TDDFT calculations, we study the nonlinear response of MgO crystal to intense incident pulses. Using infrared two-color asymmetric pulses with a duration of 18 fs and an intensity of approximately 10^{13} W/cm^2, we obtain the following results.

The generation of harmonics up to 43 eV and IAPs as short as approximately 300 as is predicted. Attosecond chirp, which is a feature of interband recombinant emissions [62], can be manipulated from positive to negative and appears for harmonics between 15 and 21 eV; in this energy range, there is a plateau in the HHG spectrum (see, for instance, Fig. S2 in Supplemental Material [53]), and high-lying conduction bands with the Van Hove singularities are present in the band structure [24]. MgO harmonic emission shows anisotropic behavior, and the HHG emission for pulse polarization along the [100] direction is stronger. Furthermore, the efficiency of the generated IAP strongly decreases when the second-pulse polarization is not along the [100] direction. Finally, we show that the HHG efficiency drops rapidly for elliptically polarized pulses; however, it provides the possibility of easily generating elliptically polarized IAPs. The linear dependence of the cutoff energy on the driving-laser peak field is observed. In addition, the effects of the pulse ellipticity and the crystal anisotropy on the cutoff energy are discussed.

The results presented in this paper demonstrate the potential of solid-state materials in future all-solid-state attosecond technologies.

[1] A. McPherson, G. Gibson, H. Jara, U. Johann, T. S. Luk, I. A. McIntyre, K. Boyer, and C. K. Rhodes, Studies of multiphoton production of vacuum-ultraviolet radiation in the rare gases, J. Opt. Soc. Am. B **4**, 595 (1987).

[2] M. Ferray, A. L'Huillier, X. F. Li, L. A. Lompre, G. Mainfray, and C. Manus, Multiple-harmonic conversion of 1064 nm radiation in rare gases, J. Phys. B: At. Mol. Opt. Phys. **21**, L31 (1988).

[3] S. Ghimire, A. D. DiChiara, E. Sistrunk, P. Agostini, L. F. DiMauro, and D. A. Reis, Observation of high-order harmonic generation in a bulk crystal, Nat. Phys. **7**, 138 (2011).

[4] M. Hentschel, R. Kienberger, Ch. Spielmann, G. A. Reider, N. Milosevic, T. Brabec, P. Corkum, U. Heinzmann, M. Drescher, and F. Krausz, Attosecond metrology, Nature **414**, 509 (2001).

[5] F. Krausz and M. Ivanov, Attosecond physics, Rev. Mod. Phys. **81**, 163 (2009).

[6] M. Drescher, M. Hentschel, R. Kienberger, M. Uiberacker, V. Yakovlev, A. Scrinzi, T. Westerwalbesloh, U. Kleineberg, U. Heinzmann, and F. Krausz, Time-resolved atomic inner-shell spectroscopy, Nature **419**, 803 (2002).

[7] F. Calegari, D. Ayuso, A. Trabattoni, L. Belshaw, S. De Camillis, S. Anumula, F. Frassetto, L. Poletto, A. Palacios, P. Decleva, J. B. Greenwood, F. Martin, and M. Nisoli, Ultrafast electron dynamics in phenylalanine initiated by attosecond pulses, Science **346**, 336 (2014).

[8] S. Neppl, R. Ernstorfer, A. L. Cavalieri, C. Lemell, G. Wachter, E. Magerl, E. M. Bothschafter, M. Jobst, M. Hofstetter, U. Kleineberg, J. V. Barth, D. Menzel, J. Burgdörfer, P. Feulner, F. Krausz, and R. Kienberger, Direct observation of electron propagation and dielectric screening on the atomic length scale, Nature **517**, 342 (2015).

[9] M. Chini, K. Zhao, and Z. Chang, The generation, characterization and applications of broadband isolated attosecond pulses, Nat. Photon. **8**, 178 (2014).

[10] S. Ghimire and D. A. Reis, High-harmonic generation from solids, Nat. Phys. **15**, 10 (2019).

[11] J. D. Cox, A. Marini, and F. J. G. De Abajo, Plasmon-assisted high-harmonic generation in graphene, Nat. Commun. **8**, 14380 (2017).

[12] G. Vampa, B. G. Ghamsari, S. S. Mousavi, T. J. Hammond, A. Olivieri, E. Lisicka-Skrek, A. Yu Naumov, D. M. Villeneuve, A. Staudte, P. Berini, and P. B. Corkum, Plasmon-enhanced high-harmonic generation from silicon, Nat. Phys. **13**, 659 (2017).

[13] S. Han, H. Kim, Y. W. Kim, Y.-J. Kim, S. Kim, I.-Y. Park, and S.-W. Kim, High-harmonic generation by field enhanced femtosecond pulses in metal-sapphire nanostructure, Nat. Commun. **7**, 13105 (2016).

[14] M. Sivis, M. Taucer, G. Vampa, K. Johnston, A. Staudte, A. Y. Naumov, D. M. Villeneuve, C. Ropers, and P. B. Corkum, Tailored semiconductors for high-harmonic optoelectronics, Science **357**, 303 (2017).

[15] D. Franz, S. Kaassamani, D. Gauthier, R. Nicolas, M. Kholodtsova, L. Douillard, J.-T. Gomes, L. Lavoute, D. Gaponov, N. Ducros, S. Fevrier, J. Biegert, L. Shi, M. Kovacev, W. Boutu, and H. Merdji, All semiconductor enhanced high-harmonic generation from a single nanostructured cone, Sci. Rep. **9**, 1 (2019).

[16] D. Gauthier, S. Kaassamani, D. Franz, R. Nicolas, J.-T. Gomes, L. Lavoute, D. Gaponov, S. Fevrier, G. Jargot, M. Hanna, W. Boutu, and H. Merdji, Orbital angular momentum from semiconductor high-order harmonics, Opt. Lett. **44**, 546 (2019).

[17] A. Wu, S. Ghimire, D. A. Reis, K. J. Schafer, and M. B. Gaarde, High-harmonic generation from Bloch electrons in solids, Phys. Rev. A **91**, 043839 (2015).

[18] S. Hüller and J. Meyer-ter-Vehn, High-order harmonic radiation from solid layers irradiated by subpicosecond laser pulses, Phys. Rev. A **48**, 3906 (1993).

[19] N. Tancogne-Dejean, O. D. Mücke, F. X. Kärtner, and A. Rubio, Impact of the Electronic Band Structure in High-Harmonic Generation Spectra of Solids, Phys. Rev. Lett. **118**, 087403 (2017).

[20] N. Klemke, N. Tancogne-Dejean, G. M. Rossi, Y. Yang, F. Scheiba, R. E. Mainz, G. Di Sciacca, A. Rubio, F. X. Kärtner, and O. D. Mücke, Polarization-state-resolved high-harmonic spectroscopy of solids, Nat. Commun. **10**, 1319 (2019).

[21] N. Tancogne-Dejean, O. D. Mücke, F. X. Kärtner, and A. Rubio, Ellipticity dependence of high-harmonic generation in solids originating from coupled intraband and interband dynamics, Nat. Commun. **8**, 745 (2017).

[22] G. Orenstein, A. J. Uzan, S. Gadasi, T. Arusi-Parpar, M. Krüger, R. Cireasa, B. D. Bruner, and N. Dudovich, Shaping electron-hole trajectories for solid-state high harmonic generation control, Opt. Express **27**, 37835 (2019).

[23] Y. S. You, D. A. Reis, and S. Ghimire, Anisotropic high-harmonic generation in bulk crystals, Nat. Phys. **13**, 345 (2017).

[24] A. J. Uzan, G. Orenstein, A. Jimenez-Galan, C. McDonald, R. E. F. Silva, B. D. Bruner, N. D. Klimkin, V. Blanchet, T. Arusi-Parpar, M. Krüger, A. N. Rubtsov, O. Smirnova, M. Ivanov, B. Yan, T. Brabec, and N. Dudovich, Attosecond spectral singularities in solid-state high-harmonic generation, Nat. Photon. **14**, 183 (2020).

[25] M. Garg, M. Zhan, T. T. Luu, H. Lakhotia, T. Klostermann, A. Guggenmos, and E. Goulielmakis, Multi-petahertz electronic metrology, Nature **538**, 359 (2016).

[26] M. Guan, S. Hu, H. Zhao, C. Lian, and S. Meng, Attosecond control of electron dynamics in two-dimensional materials, Appl. Phys. Lett. **116**, 043101 (2020).

[27] Z. Wang, H. Park, Y. H. Lai, J. Xu, C. I. Blaga, F. Yang, P. Agostini, and L. F. DiMauro, The roles of photo-carrier doping and driving wavelength in high harmonic generation from a semiconductor, Nat. Commun. **8**, 1686 (2017).

[28] A. F. Kemper, B. Moritz, J. K. Freericks, and T. P. Devereaux, Theoretical description of high-order harmonic generation in solids, New J. Phys. **15**, 023003 (2013).

[29] M.-X. Guan, C. Lian, S.-Q. Hu, H. Liu, S.-J. Zhang, J. Zhang, and S. Meng, Cooperative evolution of intraband and interband excitations for high-harmonic generation in strained MoS$_2$, Phys. Rev. B **99**, 184306 (2019).

[30] G. Ndabashimiye, S. Ghimire, M. Wu, D. A. Browne, K. J. Schafer, M. B. Gaarde, and D. A. Reis, Solid-state harmonics beyond the atomic limit, Nature **534**, 520 (2016).

[31] E. N. Osika, A. Chacon, L. Ortmann, N. Suarez, J. A. Perez-Hernandez, B. Szafran, M. F. Ciappina, F. Sols, A. S. Landsman, and M. Lewenstein, Wannier-Bloch Approach

to Localization in High-Harmonics Generation in Solids, Phys. Rev. X **7,** 021017 (2017).

[32] J. Li, X. Ren, Y. Yin, K. Zhao, A. Chew, Y. Cheng, E. Cunningham, Y. Wang, S. Hu, Y. Wu, M. Chini, and Z. Chang, 53-attosecond X-ray pulses reach the carbon K-edge, Nat. Commun. **8,** 186 (2017).

[33] K. Zhao, Q. Zhang, M. Chini, Y. Wu, X. Wang, and Z. Chang, Tailoring a 67 attosecond pulse through advantageous phase-mismatch, Opt. Lett. **37,** 3891 (2012).

[34] E. Goulielmakis, M. Schultze, M. Hofstetter, V. S. Yakovlev, J. Gagnon, M. Uiberacker, A. L. Aquila, E. M. Gullikson, D. T. Attwood, R. Kienberger, F. Krausz, and U. Kleineberg, Single-cycle nonlinear optics, Science **320,** 1614 (2008).

[35] G. Sansone, E. Benedetti, F. Calegari, C. Vozzi, L. Avaldi, R. Flammini, L. Poletto, P. Villoresi, C. Altucci, R. Velotta, S. Stagira, S. De Silvestri, and M. Nisoli, Isolated single-cycle attosecond pulses, Science **314,** 443 (2006).

[36] T. Gaumnitz, A. Jain, Y. Pertot, M. Huppert, I. Jordan, F. Ardana-Lamas, and H. J. Wörner, Streaking of 43-attosecond soft-X-ray pulses generated by a passively CEP-stable mid-infrared driver, Opt. Express **25,** 27506 (2017).

[37] H. Merdji, T. Auguste, W. Boutu, J.-P. Caumes, B. Carre, T. Pfeifer, A. Jullien, D. M. Neumark, and S. R. Leone, Isolated attosecond pulses using a detuned second-harmonic field, Opt. Lett. **32,** 3134 (2007).

[38] Y. Ding, Z. Huang, D. Ratner, P. Bucksbaum, and H. Merdji, Generation of attosecond x-ray pulses with a multi-cycle two-color enhanced self-amplified spontaneous emission scheme, Phys. Rev. ST Accel. Beams **12,** 060703 (2009).

[39] *Strong Field Laser Physics*, edited by T. Brabec (Springer, New York, 2009).

[40] W. Chen, G. Chen, and D. E. Kim, Two-color field for the generation of an isolated attosecond pulse in water-window region, Opt. Express **19,** 206010 (2011).

[41] T. T. Luu and H. J. Worner, Observing broken inversion symmetry in solids using two-color high-order harmonic spectroscopy, Phys. Rev. A **98,** 041802(R) (2018).

[42] O. Raz, O. Pedatzur, B. D. Bruner, and N. Dudovich, Spectral caustics in attosecond science, Nat. Photon. **6,** 170 (2012).

[43] C. Liu, M. Reduzzi, A. Trabattoni, A. Sunilkumar, A. Dubrouil, F. Calegari, M. Nisoli, and G. Sansone, Carrier-Envelope Phase Effects of a Single Attosecond Pulse in Two-Color Photoionization, Phys. Rev. Lett. **111,** 123901 (2013).

[44] T. Siegel, R. Torres, D. J. Hoffmann, L. Brugnera, I. Procino, A. Zair, J. G. Underwood, E. Springate, I. C. E. Turcu, L. E. Chipperfield, and J. P. Marangos, High harmonic emission from a superposition of multiple unrelated frequency fields, Opt. Express **18,** 6853 (2010).

[45] H.-C. Bandulet, D. Comtois, E. Bisson, A. Fleischer, H. Pepin, J.-C. Kieffer, P. B. Corkum, and D. M. Villeneuve, Gating attosecond pulse train generation using multicolor laser fields, Phys. Rev. A. **81,** 013803 (2010).

[46] E. Runge and E. K. U. Gross, Density-Functional Theory for Time-Dependent Systems, Phys. Rev. Lett. **52,** 997 (1984).

[47] R. van Leeuwen, Causality and Symmetry in Time-Dependent Density-Functional Theory, Phys. Rev. Lett. **80,** 1280 (1998).

[48] N. Tancogne-Dejean, M. J. T. Oliveira, X. Andrade, H. Appel, C. H. Borca, G. Le Breton, F. Buchholz, A. Castro, S. Corni, A. A. Correa, *et al.*, Octopus, a computational framework for exploring light-driven phenomena and quantum dynamics in extended and finite systems, J. Chem. Phys. **152,** 124119 (2020).

[49] E. Sejdic, I. Djurovic, and J. Jiang, Time-frequency feature representation using energy concentration: An overview of recent advances, Digital Signal Process. **19,** 153 (2009).

[50] C. Hartwigsen, S. Goedecker, and J. Hutter, Relativistic separable dual-space Gaussian pseudopotentials from H to Rn, Phys. Rev. B **58,** 3641 (1998).

[51] D. Waroquiers, A. Lherbier, A. Miglio, M. Stankovski, S. Ponce, M. J. T. Oliveira, M. Giantomassi, G.-M. Rignanese, and X. Gonze, Band widths and gaps from the tranblaha functional: Comparison with many-body perturbation theory, Phys. Rev. B **87,** 075121 (2013).

[52] The experimental feasibility of the proposed laser parameters is studied on a mid-infrared chirped-pulse optical parametric amplifier with three to four optical cycles by the group of H.M.. Femtosecond pulses exhibit extremely large spectra. For example, at his facility, a 25-fs-pulse mid-infrared beam is centered at 2 μm (6.75-fs-long optical cycles will extend approximately from 1.75 to 2.25 μm). Its second harmonic can be easily generated with use of a β-barium borate crystal. Then, this spectrum can be further broadened and compressed. After broadening of the spectrum, a specific filter can be used to tune (or truncate) the center of the spectrum by any amount. Finally, the polarization state of such a beam can be controlled on the single optical level using, for example, a TWINS (Translating Wedge based Identical pulses eNcoding System) interferometer setup.

[53] See Supplemental Material at http://link.aps.org/supplemental/10.1103/PhysRevApplied.15.014013 for further information.

[54] Y. Mairesse, A. de Bohan, L. J. Frasinski, H. Merdji, L. C. Dinu, P. Monchicourt, P. Breger, M. Kovacev, R. Taieb, B. Carre, H. G. Muller, P. Agostini, and P. Salieres, Attosecond synchronization of high-harmonic soft X-rays, Science **302,** 1540 (2003).

[55] F. Tran and P. Blaha, Accurate Band Gaps of Semiconductors and Insulators with a Semilocal Exchange-Correlation Potential, Phys. Rev. Lett. **102,** 226401 (2009).

[56] T.-J. Shao, L.-J. Lü, J.-Q. Liu, and X.-B. Bian, Quantum path interferences and selection in interband solid high-order harmonic generation in MgO crystals, Phys. Rev. A **101,** 053421 (2020).

[57] Z. Guan, X.-X. Zhou, and X.-B. Bian, High-order-harmonic generation from periodic potentials driven by few-cycle laser pulses, Phys. Rev. A **93,** 033852 (2016).

[58] G. Vampa, C. R. McDonald, G. Orlando, P. B. Corkum, and T. Brabec, Semiclassical analysis of high harmonic generation in bulk crystals, Phys. Rev. B **91,** 064302 (2015).

[59] T. Higuchi, M. I. Stockman, and P. Hommelhoff, Strong-Field Perspective on High-Harmonic Radiation from Bulk Solids, Phys. Rev. Lett. **113,** 213901 (2014).

[60] D. Ayuso, A. Jimenez-Galan, F. Morales, M. Ivanov, and O. Smirnova, Attosecond control of spin polarization in electron-ion recollision driven by intense tailored fields, New J. Phys. **19**, 073007 (2017).

[61] D. B. Milosevic, Possibility of introducing spin into atto-science with spin-polarized electrons produced by a bichro-matic circularly polarized laser field, Phys. Rev. A **93**, 051402(R) (2016).

[62] J. Li, J. Lu, A. Chew, S. Han, J. Li, Y. Wu, H. Wang, S. Ghimire, and Z. Chang, Attosecond science based on high harmonic generation from gases and solids, Nat. Commun. **11**, 2748 (2020).